Optimality of human movement under natural variations of visual–motor uncertainty

Sergei Gepshtein Laboratory for Perceptual Dynamics, Brain Science Institute, Saitama, Japan

Anna Seydell Department of Psychology, Giessen University, Giessen, Germany

Julia Trommershäuser Department of Psychology, Giessen University, Giessen, Germany

Biological movements are prone to error. Different movements lead to different errors, and the distributions of errors depend on movement amplitude and direction. Movement planning would benefit from taking this variability into account, by applying appropriate corrections for movements associated with the different shapes and sizes of error distributions. Here we asked whether the human nervous system can do so. In a game-like task, participants performed rapid sequences of goal-directed pointing movements in different directions, toward stimulus configurations presented at different eccentricities on a slanted touch screen. The task was to accumulate rewards by hitting target regions and to minimize losses by avoiding penalty regions. The distributions of endpoint errors varied in size and degree of anisotropy across stimulus locations. Our participants adjusted their movements toward the different locations accordingly. We compared human behavior with the optimal behavior predicted by ideal movement planner maximizing expected gain. In most cases, human behavior was indistinguishable from optimal. This is evidence that human movement planning approaches statistical optimality by representing the task-relevant movement variability.

Keywords: optimality, uncertainty, anisotropy, sensorimotor control, maximal gain, normative model, payoff, vision, action, surface slant

Citation: Gepshtein, S., Seydell, A., & Trommershäuser, J. (2007). Optimality of human movement under natural variations of visual–motor uncertainty. *Journal of Vision, 7*(5):13, 1–18, http://journalofvision.org/7/5/13/, doi:10.1167/7.5.13.

Introduction

We live in an uncertain world. Not only is our perception of the state of affairs in the world imperfect because of the sensory uncertainty, but we are also uncertain about the consequences of our intended actions. Even in such a simple task as rapidly reaching for the same spot with the index finger, we will inadvertently make small but different errors on every trial.

In spite of this variability, recent experimental evidence suggests that human behavior is remarkably efficient, and in many cases it is close to optimal. In these studies, human perceptual and motor behavior proved similar to predictions made by the normative models that compute best possible strategies for behavior under uncertainty ("ideal observers" and "ideal movement planners"). This evidence implies that the human nervous system can take into account ("represent") task-relevant uncertainties to optimize behavior.

For example, the human capacity to combine information from different sensory modalities (e.g., vision and touch: Ernst & Banks, 2002, Gepshtein & Banks, 2003; vision and hearing: Alais & Burr, 2004) was well predicted by an ideal observer that combines signals from different modalities according to their reliability. The computation of reliabilities requires the ability to estimate the uncertainties associated with the sensory signals, separately for each modality. The observed similarity of human and optimal behavior suggests that humans represent sensory uncertainties just as the ideal observer does.

In a similar vein, studies of movement planning showed that human performance can be successfully predicted by an ideal movement planner maximizing expected gain (Trommershäuser, Maloney, & Landy, 2003). Just as the ideal planner, humans chose strategies that maximized expected gain by minimizing the risk of possible losses due to the unavoidable noise in the execution of speeded movements (Harris & Wolpert, 1998). To achieve such optimality, the neural mechanism of movement planning must be able to represent some characteristics of motor errors (Diedrichsen, Hashambhoy, Rane, & Shadmehr, 2005; Scheidt, Conditt, Secco, & Mussa-Ivaldi, 2005).

The evidence of optimal motor behavior under uncertainty comes from experiments in which humans were making repetitive hand movements that differed very little in amplitude and direction across trials (e.g., Trommershäuser et al., 2003). Thus, the distributions of

doi: 10.1167/7.5.13 Received November 10, 2006; published September 28, 2007 ISSN 1534-7362

sensorimotor errors associated with movements over the long stretches of trials were roughly invariant. The results of these studies led to the conclusion that the human nervous system represents some characteristics of sensorimotor uncertainties to optimize behavior. But does this evidence imply that biological movements under natural conditions are also optimized by taking into account the estimates of sensorimotor uncertainty?

Everyday motor behavior of animals and humans consists of sequences of movements over different distances and in different directions, invoking error distributions of different sizes and shapes. In contrast, in the laboratory tasks described above, participants had an unusual opportunity to explore and learn the errors associated with specific movements. This concern is aggravated by recent results showing that humans could quickly learn new sensorimotor uncertainties in the repetitive-movement paradigm, when visual feedback about the repetitive movement was altered by the experimenters (Trommershäuser, Gepshtein, Maloney, Landy, & Banks, 2005).

In this study, we investigated whether the human nervous system can sustain optimal behavior under more challenging conditions. We studied how humans performed rapid sequences of movements while individual movements differed with respect to the shapes and the sizes of error distributions. Optimal behavior in these conditions does not only require representing properties of error distributions, but also representing many different error distributions associated with different movements. Thus, we identify two questions:

1. *Shapes of error distributions*. For planar two-joint arm movements, the distribution of errors is larger in the direction of movement than in other directions: It is anisotropic (Gordon, Ghilardi, & Ghez, 1994; van Beers, Haggard, & Wolpert, 2004). Can the nervous system represent anisotropic error distributions?

2. *Number of error distributions*. In actions that consist of movement sequences, different uncertainties affect behavior in rapid succession. Can the nervous system represent several different shapes of error distributions and rapidly access them to optimize action?

Here we studied human active behavior using a laboratory task that allowed us to address both questions:

i. Participants executed movements in four different directions and over two distances, which led to error distributions of substantially different shapes and sizes.

ii. Movements invoking different error distributions followed one another in rapid random succession.

To sustain optimal behavior for the different locations, the nervous system has to represent several error distributions concurrently, or it has to rapidly switch from one representation to another. We found that participants adjusted their movements according to the shapes and sizes of their error distributions at the different locations; in many cases, human behavior was indistinguishable from optimal, indicating that humans can represent different shapes of anisotropic error distributions, and also rapidly access these representations, to optimize movement sequences associated with the different distributions.

Methods

Apparatus

The experiments were run on a Dell Precision PWS 380 computer using Python® programming language. Participants were seated in front of a monitor on which we mounted a touch screen (AccuTouch, Elo Touchsystems®). The precision of the touch screen was constant across the screen: For mouse clicks, the average standard deviation was approximately 0.5 mm, for touches with the index finger it was less than 1.5 mm for all target locations. Because the measurement errors are constant across screen locations, any differences in distributions of movement endpoints by human participants measured at different screen locations must arise from different human behavior at these locations.

The monitor with the touch screen could be slanted by any angle (Figure 1). We used two magnitudes of slant: In one condition ("slant 0"), the screen was orthogonal to the gaze line to the center of the screen; that is, the angle between the screen and the gaze-normal plane was 0°. In the other condition ("slant 53"), the screen was parallel to the floor, subtending 53° from the gaze-normal plane. We used a chin rest to keep the viewing distance to the dock at 52 cm for both slants of the screen.

Stimuli, procedure, and experimental design

A small bright disc at screen center ("dock"; radius 10 pixels/3 mm) was the starting position for the finger in every trial. Participants initiated trials by touching the dock, which initiated presentation of a stimulus configuration at one of the eight locations arranged around the dock on two concentric rings with radii 3 and 12 cm (3.3° and 13.2° of visual angle, respectively; see Figure 2).

Each stimulus consisted of two colored regions: a "target" disk (green) and a nearby "penalty" disk (red), displayed on a gray background. The overlap of target and penalty region was shown in yellow. Target and penalty region had the same radius R (20 pixel/6 mm). As shown in Figure 2, the centers of adjacent targets and penalties were always separated by R, either along the dock–target axis ("aligned" condition) or in the direction orthogonal to the dock–target

axis ("nonaligned" conditions). There were three possible locations of the penalty relative to each target, but only one target and one penalty were presented on every trial.

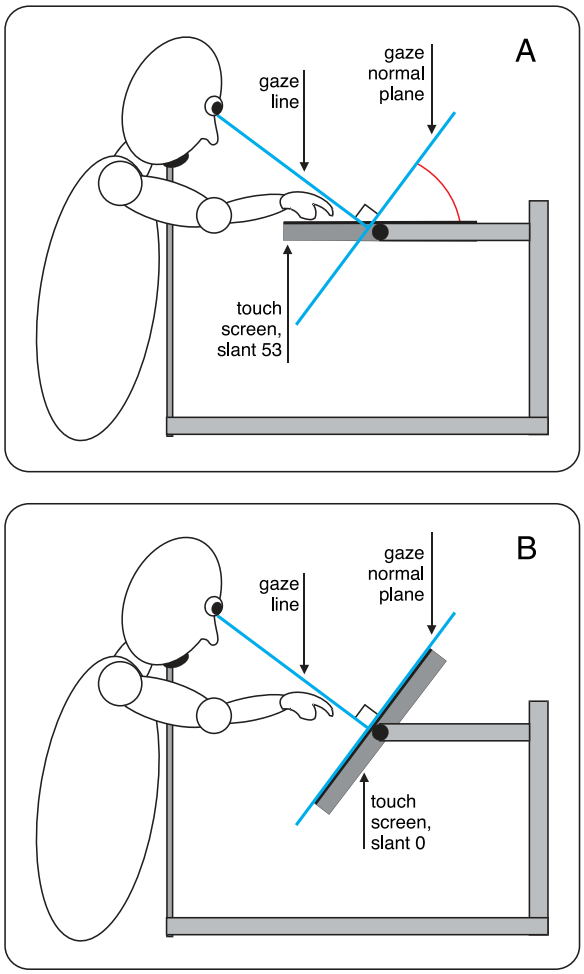

Figure 1. Experimental apparatus. The viewing distance to screen center was fixed at 52 cm; a chin rest was used to stabilize head position. The screen was slanted either 53° ("slant 53" condition; panel A) or 0° ("slant 0" condition; panel B) relative to the gaze-normal plane. Participants performed speeded pointing movements with their right index finger (panel C).

The time limit to complete the movement, that is, to hit the screen again following movement initiation, was 650 ms. The part of the stimulus that was hit within the 650 ms after stimulus onset remained on the screen until the dock was hit again. If the region where the target and penalty overlapped was hit, then both target and penalty regions remained on the screen until the next hit of the dock. The point of contact of the finger on the screen ("endpoint" of movement) was marked by a small dark-red dot (radius of 7 pixels/2.1 mm) and was displayed on the screen until the dock was hit again.

Hits within the target and penalty region led to explicit rewards and losses that accumulated across trials. Each hit into the target increased the score by 1 point (reward), and each hit into the penalty region decreased the score by

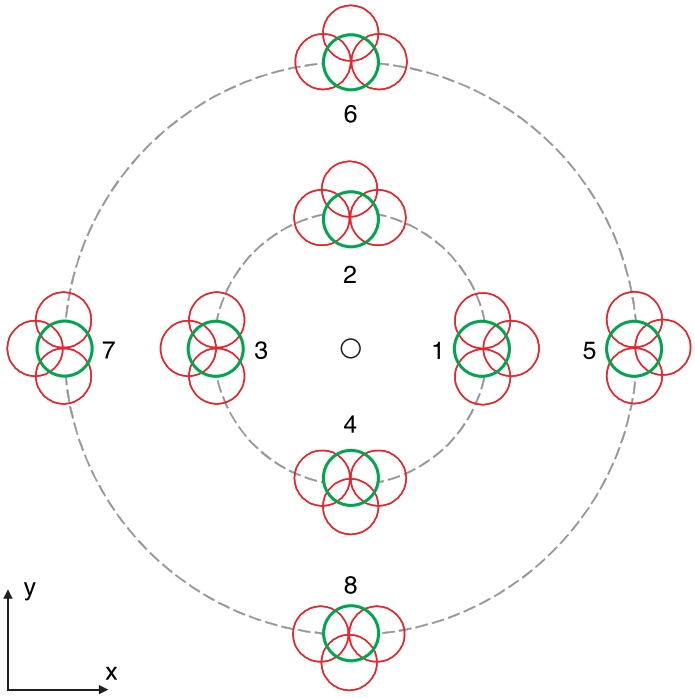

Figure 2. Stimulus configurations. Participants started every trial by hitting a central circle ("dock"), which initialized stimulus presentation. Each stimulus consisted of one "target" (a green disk) and one adjacent "penalty" (a red disk) at one of the eight locations. The targets could appear at one of two distances from the dock, indicated by the two dashed circles, the "inner ring" and the "outer ring." The red circles represent three possible positions of penalties relative to each target. In the "aligned" condition, the target–penalty axis was aligned with the dock–target axis, and in the two "nonaligned" conditions the target–penalty axis was orthogonal to the dock–target axis. This resulted in 24 target–penalty configurations in total: three configurations at each of the eight locations. (The stimulus configurations as displayed here are not to scale. In the actual stimulus display, the radius of the outer ring of targets was four times larger than the radius of the inner ring; see also Figure 6.)

2 points (loss). Hits into the overlap of target and penalty region scored both the reward and loss (1 point subtracted from the cumulative score). Hits outside the target or the penalty region and late hits (after the time limit expired) did not change the score. The cumulative score was continuously displayed in the lower left corner of the screen and was updated after each trial.

Participants first trained in a 400-trial session with zero penalty in the slant 0 condition to learn the time requirements of the speeded pointing task. After the training session, participants completed 16 sessions of 400 trials each. Slant of the touch screen and penalty value were held constant across the 400 trials of each session. Within one session, each of the eight target locations was presented 50 times, in random order, and one of the three possible locations of the penalty region relative to the target was chosen randomly in each trial.

For each slant condition, every participant first did two sessions with zero penalty, followed by six sessions with nonzero penalty. The two slant conditions were randomized across participants and conditions.

Participants and instructions

Two males and five females (ages 23–37) participated in the experiment. The participants were four students at the University of Giessen and the three authors. All participants were right-handed and had normal or corrected-to-normal vision. The naive participants had given their informed consent before testing and were paid for their participation. They were unaware of the hypothesis under test. Before each block of trials, participants were informed of the target and penalty values. The only instruction was to accumulate as many points as possible. Participants received no explicit instruction on where to aim.

Data analysis

For each trial, we recorded response time (defined as the period between the hit of the dock and the next hit of the screen), hit location, and the score. Trials in which participants initiated movements later than 400 ms after the stimulus onset, or completed the movement later than 650 ms after stimulus onset, were excluded from the analysis. Data points that were farther than 2.5 target radii (15 mm) from the target center were classified as outliers and were excluded from the analysis. (In total, 7% of trials were excluded from the analysis because they were classified as outliers and because of the timeout.)

Each participant completed approximately 4,800 trials during the 12 nonzero penalty sessions of the experiment, yielding approximately 100 repetitions per stimulus configuration. Movement endpoints were recorded and are reported relative to the center of the target circle.

Computation of endpoint errors

We analyzed endpoint errors separately for each participant, screen slant, and stimulus configuration (i.e., separately for each target location and each penalty location relative to the target). In the nonzero penalty conditions, each of the endpoint distributions contained approximately 100 data points. Because previous studies have shown that in tasks similar to ours the distributions of endpoints are well fit by the bivariate Gaussian distribution (e.g., Trommershäuser et al., 2005), we computed standard error ellipses for each stimulus configuration by fitting bivariate Gaussian distributions to the measured distributions of endpoints. We assumed that participants select a single aim point per stimulus configuration, and that the endpoints deviate from the aim point across trials because of planning and execution noise.

We defined the "aim point" of error distribution as the mean of the fitted bivariate endpoint distribution (Figure 3). Following Gordon et al. (1994), we refer to errors along the direction of movement as "extent errors" and to errors orthogonal to the direction of movement as "directional errors" (Figure 3).

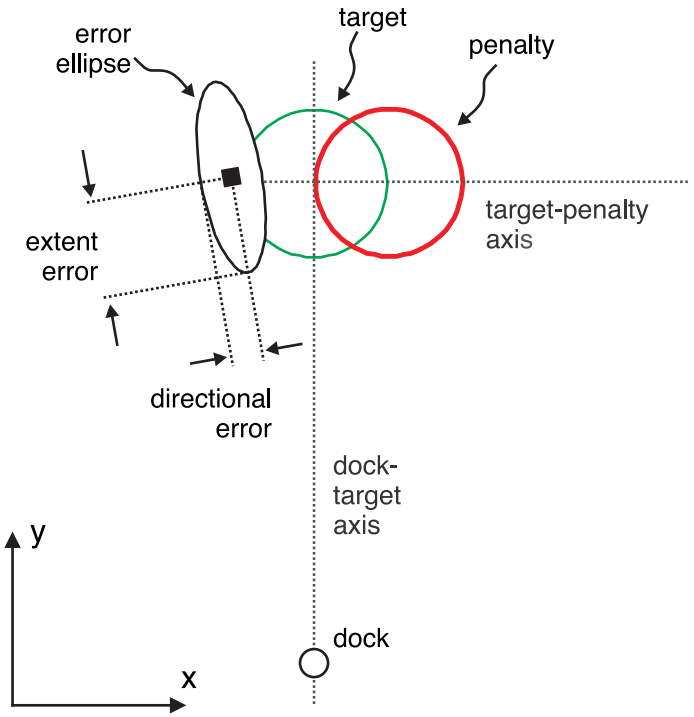

Figure 3. Endpoint error anisotropy. The "error ellipse" represents a bivariate distribution of endpoint errors. The black square inside the ellipse represents the aim point, which is the mean of the endpoint error distribution. The "extent error" is measured by the standard deviation of the endpoint error distribution along the direction of movement. The "directional error" is measured by the standard deviation along the orthogonal orientation, that is, away from the direction of movement. This diagram illustrates a "nonaligned condition" in which the dock–target axis and the target–penalty axis are orthogonal to each other (see also Figure 2).

Absolute magnitude of endpoint error

We measured the absolute magnitude of endpoint error, that is, the size of the error ellipse, by computing the square root of the determinant of the error distribution covariance matrix ($|\Sigma|^{1/2}$).

Anisotropy of endpoint error

We quantified the degree of anisotropy of each endpoint distribution by computing its index of anisotropy $L = \lambda_1/\lambda_2$, where λ_1 is the eigenvalue associated with the principle component of the distribution, and λ_2 is the eigenvalue associated with the second component. This index of anisotropy L quantifies the elongation of the endpoint error distribution, such that the larger the index, the larger the elongation of the distribution, that is, for isotropic (circular) distributions $L = 1$, and for anisotropic distributions $L > 1$.

Effect of anisotropy of endpoint error

We expected larger shifts of aim points from the target center in the conditions in which the endpoint error distribution was elongated in the direction of movement, that is, along the dock–target axis (aligned compared to nonaligned conditions; see also the Predictions of the ideal planner section and Figure 4). We tested this by computing the ratios of the mean shift from the target center in the aligned and nonaligned conditions ("relative shift of aim point"; Figures 5B and 11), and by comparing the observed shifts in the aligned and nonaligned conditions (Figures 8 and 9).

Ideal planner with anisotropic motor variability

We compared human performance to the performance of an ideal movement planner maximizing expected gain ("ideal movement planner"). The model is a generalization of the model introduced by Trommershäuser et al. (2003). It determines which visuomotor strategy S—resulting in mean movement endpoint $(\bar{x}, \bar{y})$—yields the highest expected gain, taking into account the stimulus configuration, the associated gains and penalties, and the task-relevant endpoint variability.

Here we compute optimal performance under the assumption that movement endpoints $\vec{x}$ = (x,y) are distributed according to a bivariate Gaussian distribution,

$$p\left(\vec{x} \mid \vec{\mu}, \hat{\Sigma}\right) = \frac{1}{2\pi\sqrt{|\hat{\Sigma}|}} \exp\left[-\frac{1}{2}\left(\vec{x}-\vec{\mu}\right)^T \hat{\Sigma}^{-1}\left(\vec{x}-\vec{\mu}\right)\right], \quad (1)$$

where $\vec{\mu} = (\mu_x, \mu_y)$ and $|\hat{\Sigma}|$ are the mean and the determinant of the covariance matrix of the movement endpoint distribution on the screen, respectively. This means that movement endpoints are distributed around the mean endpoint $\vec{\mu}$ according to a bivariate Gaussian distribution, and λ_1 and λ_2 are the eigenvalues of the covariance matrix, representing the standard deviations in the direction of largest endpoint error and in the direction orthogonal to the direction of largest endpoint error (see also Anisotropy of endpoint error section). We will refer

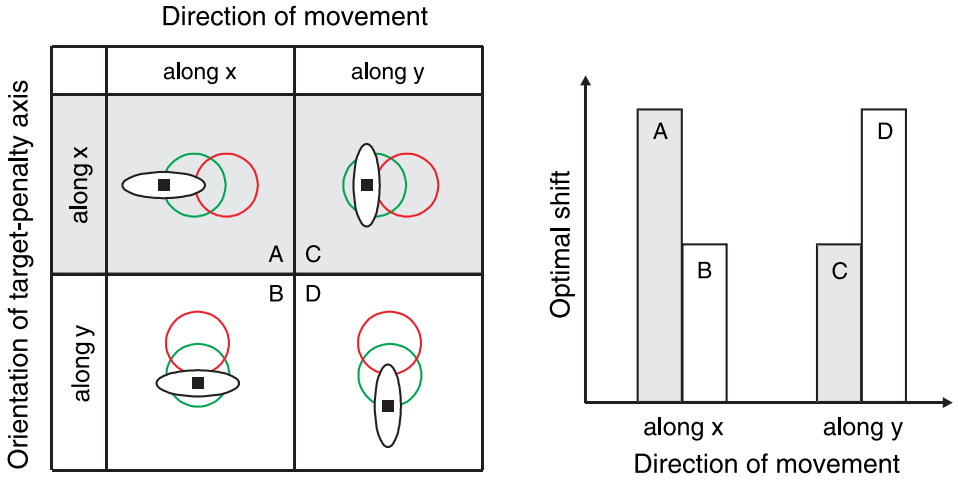

Figure 4. Qualitative illustration of the effect of endpoint error anisotropy on aiming predicted by the ideal planner. *Left panel*. Ellipses represent the anisotropy of endpoint error distributions (Figure 3), which changes as a function of movement direction: Endpoint errors are larger in the direction of movement than in the orthogonal direction (Figures 7 and 11). Black squares represent aim points, which are the means of the bivariate endpoint error distributions. *Right panel*. "Optimal shift" is the distance from target center to the aim point predicted by the ideal planner. When the axis of anisotropy is aligned with the orientation of the target–penalty axis (panels A and D), the predicted shift is larger than when the axis of anisotropy is orthogonal to the target–penalty axis (panels B and C). Thus, predicted optimal shifts for the same stimulus depend on the direction of movement toward the stimulus.

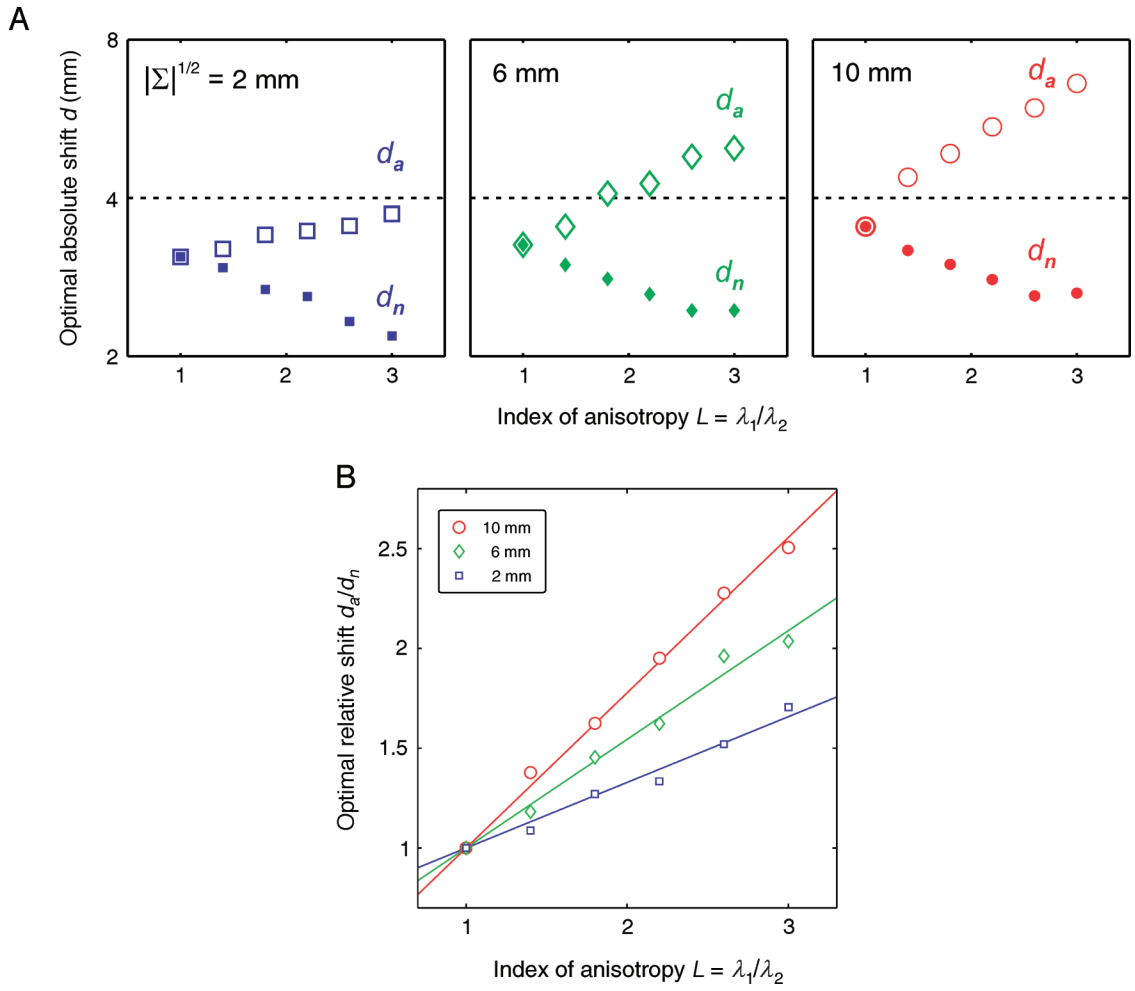

Figure 5. Predictions of the ideal planner. (A) Predicted shifts of aim point, assuming that the endpoint error ellipses are elongated parallel to the dock-to-target line: in the "aligned" (d_a; Figures 4A and 4D) and "nonaligned" (d_n; Figures 4B and 4C) conditions. The different plots correspond to different amounts of endpoint error ($|\Sigma|^{1/2}$) indicated in the top left corner of each plot. (B) Ratios of predicted shifts grow monotonically as a function of endpoint error anisotropy. The slope depends on the overall size of endpoint error: the larger the error the larger the slope. (The small deviations from the line indicate fluctuations due to Monte Carlo simulations with 10,000 repetitions per condition.)

to $\vec{\mu}$ as the "aim point." In our task, we find that the covariance matrices of the endpoint error distributions differ across target locations and target-to-penalty orientations (Figures 6, 7, 10, and S2). Therefore, the probability of hitting into a specific region R_i (i = 1,2), that is, the probability of hitting inside the target (R_1) or penalty disk (R_2), or both, when aiming for $\vec{\mu}$, varies for each target location t (t = 0,…, 7) and is defined by

$$P(R_i|\vec{\mu}_t, \hat{\Sigma}_t) = \int_{R_i} p(\vec{x}\,|\,\vec{\mu}_t, \hat{\Sigma}_t)\, dx\, dy. \quad (2)$$

In other words, the choice of aim point $\vec{\mu}_t = (\mu_{x,t}, \mu_{y,t})$ determines the probability $P(R_i|S)$ (i = 1,2) of hitting regions R_i. Here we used a single target region (gain G_1 = 1) and a single penalty region (gain G_2 = 0 or −2) per trial. The expected gain of aiming at $\vec{\mu}_t$ is then defined by

$$\mathrm{EG}(\vec{\mu}_t, \hat{\Sigma}_t) = P(R_1|\vec{\mu}_t, \hat{\Sigma}_t) * G_1 + P(R_2|\vec{\mu}_t, \hat{\Sigma}_t) * G_2. \quad (3)$$

When aiming at target location t, the optimal movement strategy is to aim at $\vec{\mu}_t^* = (\mu_{x,t}^*, \mu_{y,t}^*)$ maximizing Equation 3. (The asterisks indicate optimal strategies.) When the penalty is zero, the optimal aim point is the center of the target region. For nonzero penalties, the optimal aim point shifts away from the penalty region and therefore away from the target center. The predicted optimal shift is larger in the direction of larger endpoint variability as we show next.

Predictions of the ideal planner

Maximizing gain in our task requires shifting the aim point away from the penalty region, for a distance that depends on the shape and orientation of the endpoint distribution. In our experiments, endpoint variability differed across movements directed at different target locations and stimulus orientations. An optimal strategy in planning movements for each target location has to take into account the endpoint error distribution expected at that location. For example, when the penalty region is displayed to the right of (or above) the target, the optimal aim point is shifted left (or down) from the target center (Figure 4). The optimal shift is larger in the direction of larger endpoint variability.

To predict the optimal shifts and gains associated with each target location and stimulus orientation, we measured the endpoint distributions for each participant at each stimulus configuration (24 configurations per participant). Using these estimates, we predicted optimal aim points by performing numerical Monte Carlo simulations of the ideal planner, separately for each participant and each stimulus configuration. The simulations did an exhaustive two-dimensional search across locations in the vicinity of the target. The optimal aim point was defined as the point of highest expected gain.

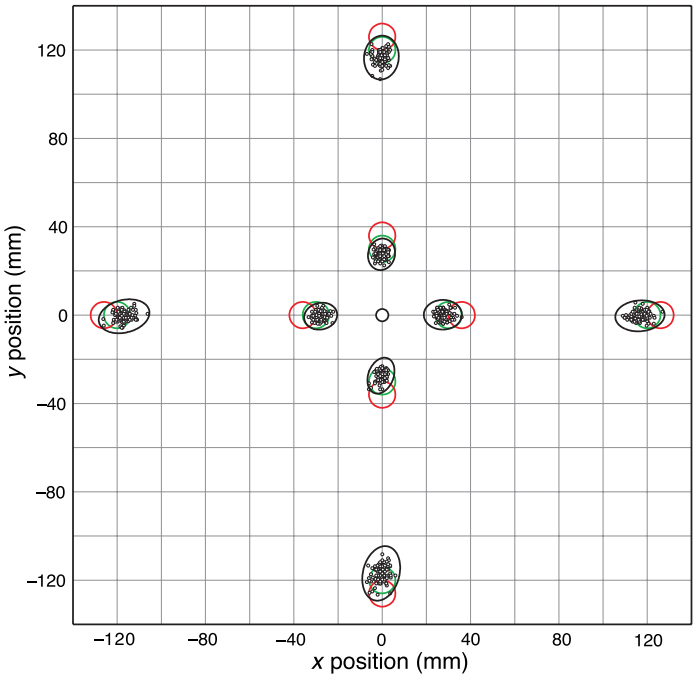

Figure 6. Observed endpoints for one participant (B.B.) in the aligned conditions at slant 0. The grid on the background represents the actual dimensions of our display. The green and the red circles represent the targets and the penalty regions as they appeared in the aligned conditions. The small black circles represent movement endpoints (in the condition in which hitting the penalty region incurred a loss of 2 points). Black ellipses mark three standard deviations of bivariate normal distributions fitted to the endpoints.

We show ideal planner predictions in more detail in Figures 5 and S1. For isotropic endpoint distributions (index of anisotropy $L = 1$), the same shifts are expected in the aligned and nonaligned conditions. For anisotropic endpoint distributions ($L > 1$), the expected shifts depend on the degree of elongation and the size of endpoint error distribution. The expected shifts are generally larger in the aligned (d_a) than nonaligned (d_n) conditions. This effect is larger for more anisotropic error distributions, as shown in the three panels of Figure 5A. The difference between optimal shifts in the aligned and nonaligned condition increases with the size of endpoint distribution (Figure 5B). The effects of anisotropy and size of endpoint error distributions on the predicted optimal shift are separable (Figure S1).

Comparison of observed and optimal behavior

To measure efficiency of human movements, we compared observed aim points to the aim points predicted by an ideal movement planner (see next section for a definition of the "ideal planner"). We define shift efficiency E_S as the normalized difference of the observed shift from the target center d_{obs} and the optimal shift from the target center d_{opt}, $1 - |d_{obs} - d_{opt}|/d_{opt}$.

We also compared participants' average winnings to the winnings predicted by the ideal movement planner. We define gain efficiency E_G as $1 - (G_{opt} - G_{obs}) / G_{opt}$, where G_{obs} is the actual (observed) gain collected by a participant and G_{opt} is the optimal gain predicted by the ideal planner (Equation 3) for that participant using his or her measured distribution of endpoint errors at every condition.

We compared human and predicted performance using a χ^2 test of goodness of fit. The results of this comparison are reported in Table 2.

Results

Endpoint error distributions vary as a function of movement direction

Movement kinematics and the distributions of movement endpoints varied significantly across target locations. Movement amplitude and direction both affected endpoint errors, whereas the slant manipulation had a negligible effect. The sizes and shapes of endpoint distributions changed as a function of movement distance from the dock to targets.

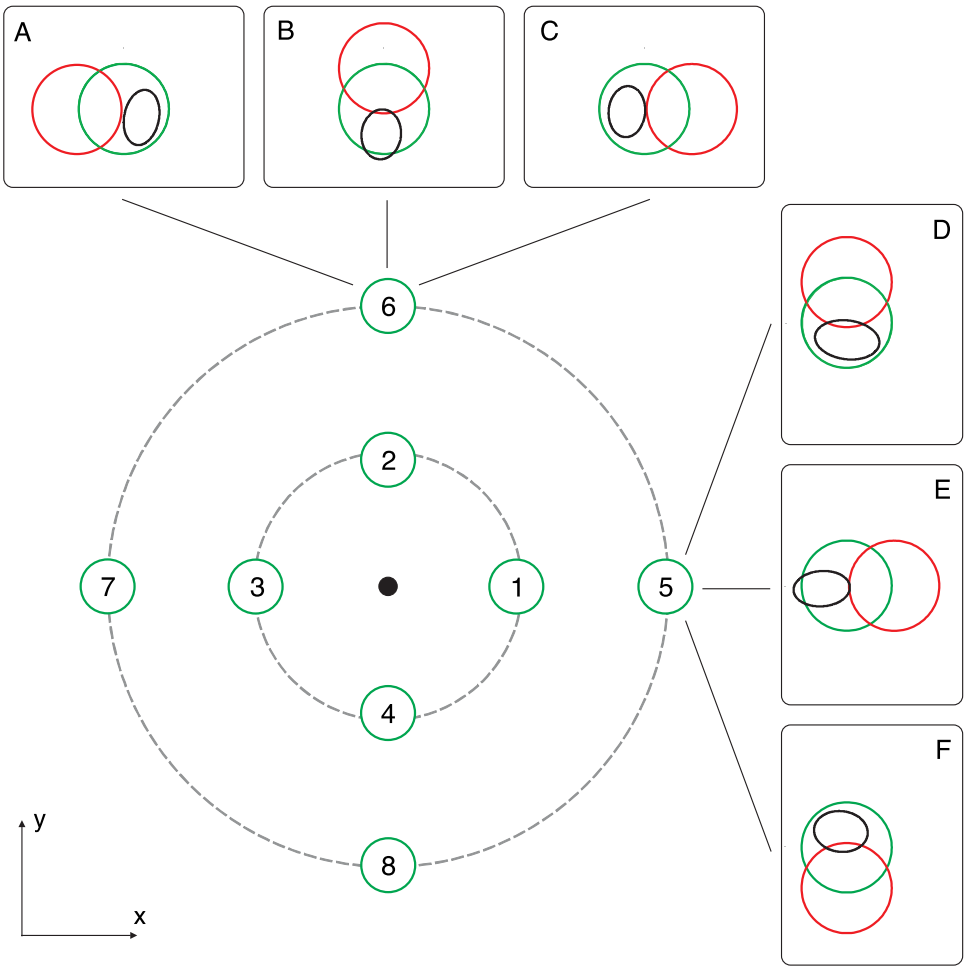

Figure 7. Endpoint error ellipses at two target locations. The green circles represent targets at the eight stimulus locations. The ellipses in panels A–F represent endpoint distributions for participant B.B., at slant 0, at three locations of penalty regions adjacent to Target 5 (D–F) and Target 6 (A–C). The ellipses illustrate the anisotropy of the endpoint error distributions; they are one standard deviation contours of Gaussian fits to the endpoint error distributions for each stimulus configuration (see Methods section). The axis of elongation is the *Y*-axis for Target 6 and the *X*-axis for Target 5, corresponding to the directions of movement to the two targets.

Response times

Response times of movements from the dock to the inner ring were significantly shorter than those of movements from the dock to the outer ring. (Note that in our task, response time is the time elapsed between hitting the dock and the next hit of the screen, close to or inside the target area.) At slant 0, the average response time for outer-ring movements (581 ± 44 ms) was significantly longer than for inner ring movements, which took 489 ± 63 ms (t = 13.0, $p < .001$). For slant 53, movement times were, respectively, 610 ± 39 and 511 ± 59 ms; they also differed significantly (t = 12.31; $p < .001$). Although the distance to the outer ring was four times the distance to the inner ring, response times to the outer-ring targets were less than four times the response times to inner-ring targets. Assuming that reaction times for targets on the outer ring did not significantly differ from those for the outer ring, this result indicates that movements to the outer ring were performed at higher average speeds.

We compared endpoint errors at different target locations and stimulus orientations by analyzing the shapes and the sizes of the corresponding endpoint error distributions. We computed standard error ellipses for each configuration by fitting bivariate Gaussian distributions to the distributions of endpoints (Figure 6). Examples of one standard error ellipses from one participant (B.B.) are displayed in Figure 7.

For stimulus locations above and below the dock, error ellipses were elongated along the *Y*-axis. By contrast, for stimulus locations to the right and to the left of the dock, ellipses were elongated along the *X*-axis (illustrated schematically in Figure 8). To evaluate the degree of anisotropy, we aligned the endpoint error distributions within a ring of targets by superimposing the directions of movement (following Gordon et al., 1994) and performed Bartlett's tests for homogeneity of variance (Table 1). The hypothesis of homogeneous variance was violated at the confidence level of .05 for all participants, conditions, and slants.

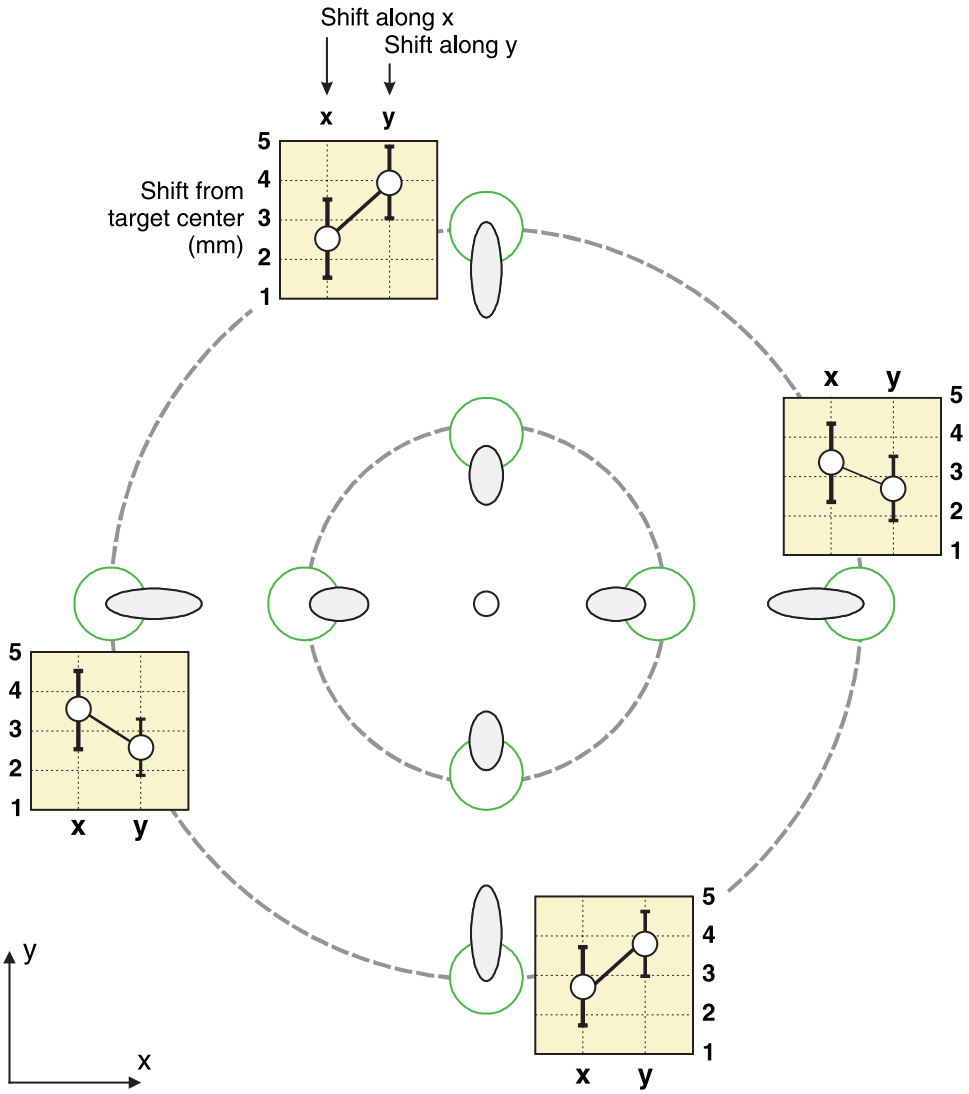

Figure 8. Effects of the shape of endpoint distribution on the shift of aim point, at slant 0. The green circles represent targets at the eight stimulus locations. The gray ellipses schematically represent the sizes and the shapes of endpoint error distributions: The distributions are more anisotropic (more elongated in the direction of movement; Figure 11), and their dispersion is larger, on the outer than on the inner ring of targets. In the graphs shown next to the outer-ring targets, we plot the measured shifts of aim points from the target center, averaged across the seven participants. (The error bars are ±1 *SE* of the average.) Labels "x" and "y" indicate the shifts in *x* and *y* directions, respectively, for trials where penalties were presented to the left and to the right of the targets ("*x*") or above and below the targets ("*y*"). Evidently, on the outer rings of targets, the shifts aligned with movement orientation (and consequently with the elongation of endpoint distribution) were larger than the shifts orthogonal to that orientation.

We compared the *magnitude* of the endpoint error for movements toward the inner and the outer ring of targets by computing the square root of the determinant of the endpoint error distribution covariance matrix $|\Sigma|^{1/2}$ (for details, see Methods section). Results are reported in Table 1. The endpoint error was larger on the outer ring than on the inner ring of targets by a factor of 1.89 (paired $t = 5.77$, $p = .001$) for slant 0, and by a factor of 2.19 (paired $t = 6.46$, $p < .001$) for slant 53.

We quantified the anisotropy of endpoint error distributions by computing the index of anisotropy (see Methods section). Results of this computation are shown on the horizontal axis of Figure 11—separately for each participant, screen slant, and ring of targets. For most participants, the anisotropy of endpoint error distributions was larger on the outer than on the inner ring, at both slants. On average, the outer-ring anisotropy was larger than the inner-ring anisotropy by a factor of 1.22 (paired $t = 4.41$, $p = .003$) for slant 0, and by a factor of 1.24 (paired $t = 4.25$, $p = .004$) for slant 53. (The χ^2 values reported in Table 1 further support this finding.)

	Inner ring (Targets 1–4)			Outer ring (Targets 5–8)		
	p	χ^2	$\lvert\Sigma\rvert^{1/2}$	p	χ^2	$\lvert\Sigma\rvert^{1/2}$
A.S.	<.0001	76.50	2.07	<.0001	156.30	3.90
J.T.	.0003	16.32	2.36	<.0001	133.77	4.32
B.B.	<.0001	42.04	4.09	<.0001	166.85	6.87
D.T.	<.0001	46.09	4.29	<.0001	148.84	7.30
A.T.	.0152	8.38	4.08	<.0001	81.22	8.45
T.M.	<.0001	22.82	3.53	<.0001	113.00	5.78
S.G.	<.0001	50.25	4.17	<.0001	145.27	9.93

Table 1. Results of Bartlett's test for homogeneity of endpoint variance, at slant 0. For every participant and ring of targets, we aligned the means of the endpoint distributions and rotated the distributions such as to align the dock-to-target orientations. We then tested whether the variances of resulting endpoint error distributions along the two principal components were equal. The small p values and large χ^2 values indicate the failure of the hypotheses that the variances were equal. Estimates of the amount of endpoint error ($\lvert\Sigma\rvert^{1/2}$) for the two rings of targets indicate that the endpoint error was larger on the outer than on the inner ring. (Results for slant 53 are shown in Table S1.)

Humans compensate for changes in the shape of endpoint variability

As we pointed out above (Ideal planner with anisotropic motor variability), the optimal shifts of aim point are larger in the aligned than nonaligned conditions, when the error ellipses are elongated parallel to the dock–target axis (Figures 4 and 5). As we show in Figures 8 and 9, human data are consistent with this prediction on the outer ring of targets, where the anisotropy of endpoint variability is larger than on the inner ring. At slant 0, for movements to targets above and below the dock, where endpoint distributions were elongated in y-direction, the shifts of aim point were larger in y-direction than in x-direction (t = 7.24, p < .001; Figure 8). For movements toward targets to the left and the right of the dock, where endpoint distributions were elongated in x-direction, the shifts of aim point were smaller in y-direction than in x-direction (t = 4.12, p = .012; Figure 8). At slant 53, a similar pattern of results was observed on the outer ring of targets. The shifts were larger in y-direction than in x-direction for targets above and below the dock (t = 5.25, p < .001). For movements toward targets to the left and to the right of the dock, the shifts were smaller in y-direction than in x-direction (t = 2.65, p = .02). This pattern was found for movements to outer-ring targets, but not to inner-ring targets.

In Figure 9, we compare the observed shifts of aim points from the target center in the aligned and the nonaligned conditions. For the outer ring of targets, the data fall off the main diagonal of the plot, indicating that shifts in the aligned conditions were larger than in nonaligned conditions, as predicted by the ideal planner (Figure 5B). For the inner ring of targets, the data fall near the main diagonal, indicating that shifts in the aligned and nonaligned conditions were similar. We found a similar pattern of results for slant 53 (not shown in Figure 9).

Orientations of error ellipses

We analyzed the orientations of endpoint error ellipses using the principle component analysis of endpoint error distribution (Figures 10 and S2). On average, the principle components were aligned with the dock–target axis. The mean orientation and circular standard deviation of the principle components for slant 0 were 2.96° and 27.50°, respectively. For slant 53, these parameters were 3.08 and 30.86. (We computed the circular standard deviation as $(180°/\pi)\sqrt{-2\ln r}$, where r is the *mean resultant length* of principle component orientations expressed in radians; Fisher, 1993.)

The variability of principle component orientations differed substantially across rings of targets (Figures 10B and 10C). At slant 0, the circular standard deviation was 36.62° on the inner ring, but on the outer ring it was only 14.80°. (The two mean orientations were 2.84° and 3.06°, respectively.) At slant 53, the circular standard deviations were 32.0° on the inner ring and 29.5° on the outer ring,

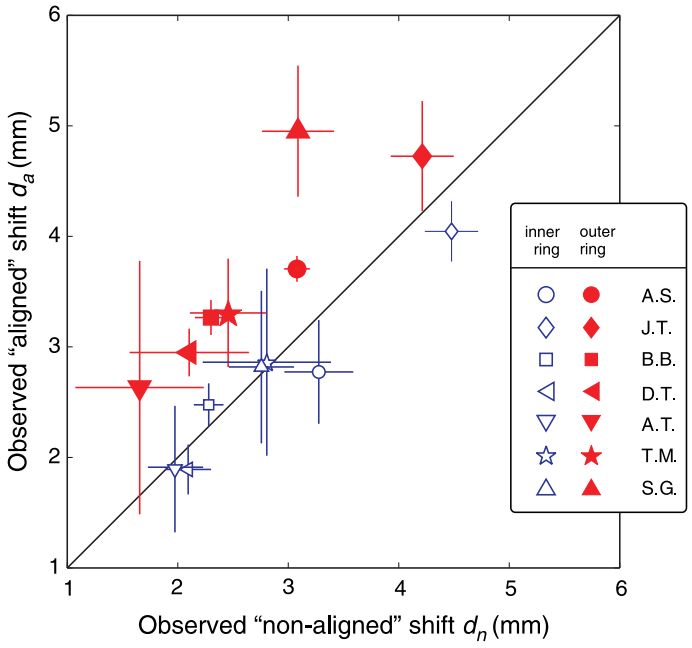

Figure 9. Observed shifts of aim point for the "aligned" compared to the "nonaligned" condition, for slant 0. For targets on the outer ring, shifts in the aligned condition are larger than in the nonaligned condition (i.e., they fall above the main diagonal), just as predicted by the ideal planner (Figure 5B). The data from the inner ring of targets fall near the main diagonal. This difference suggests that the variability of error ellipse orientations was larger on the inner ring than on the outer ring (for further detail, see text and Figure 10).

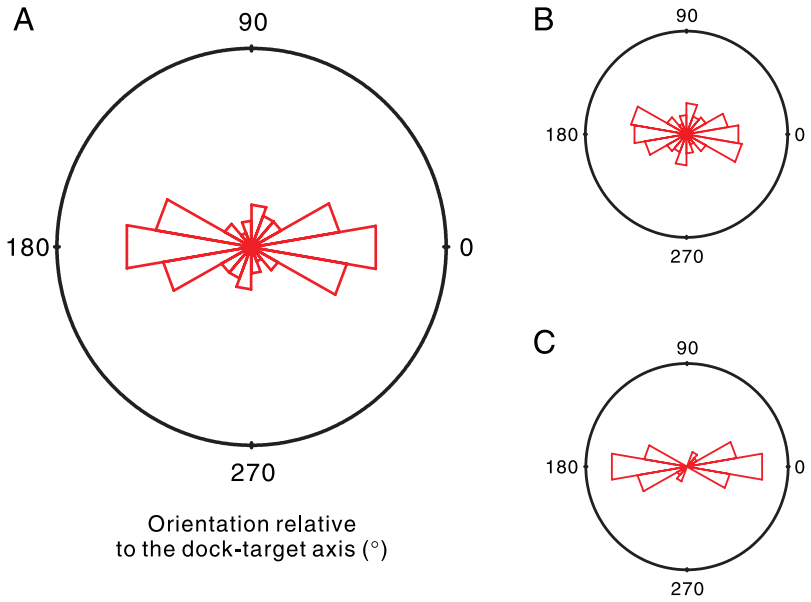

Figure 10. Rose diagrams of the orientations of principle components of endpoint error distributions for all conditions and all participants, at slant 0 (A), and separately for the inner (B) and outer (C) rings of targets at slant 0. To compare the orientations across directions of movement, we added 90° to the principle component orientations for movements along the *y*-direction. If the principal components had been perfectly aligned with the dock–target axis, they would be perfectly aligned with the 0° (180°) orientation in the diagrams. The variability of principle components was larger on the inner (B) than the outer (C) rings of targets. The diagrams for slant 53 are presented in Figure S2. (In rose diagrams, the area of each sector is proportional to the relative frequency of observations, so the radii of sectors are equal to the square root of the relative frequencies; Fisher, 1993. Every sector is replicated on the opposite side because the sectors represent orientations rather than directions.)

that is, about as large as on the inner ring at slant 0. It is important to estimate the variability of error ellipse orientations because the locations of optimal aim points predicted by the ideal planner depend on the orientation of error ellipses. For error ellipses misaligned with the dock–target axis, the ideal planner predicts a smaller difference between the shifts of aim points in the "aligned" and "nonaligned" conditions (this terminology is explained in Figure 4). We return to this issue in the next section.

We summarize the effect of endpoint error anisotropy on aiming behavior in Figure 11, where we plot the relative shifts of aim points (see Methods section), averaged within each ring of targets, separately for each participant and slant. We found significantly larger relative shifts for movements directed at the outer than the inner ring of targets. This is consistent with our finding that outer-ring anisotropy was significantly larger than the inner-ring anisotropy.

Notice that, according to the ideal-planner predictions in Figure 5B, relative shifts ought to approach 1.0 when the index of anisotropy approaches 1.0. In contrast, human inner-ring relative shifts converged to 1.0 for indices of anisotropy larger than 1.0. The reason for this discrepancy becomes clear when we take into account the observed variability of error ellipse orientations. In the simulations of the ideal planner shown in Figure 5, we assumed that error ellipses were perfectly aligned with the dock–target axis. This is not the case for human data (Figures 10 and S2), in particular for the inner ring of targets where the variability of the ellipse orientations was larger than for the outer ring. The predicted optimal shift must be smaller for endpoint error ellipses that are misaligned with the dock–target axis. We therefore repeated our analysis while taking into account the variability of error ellipse orientations. The two lines in Figure 11 are the relative shifts predicted by the ideal planner assuming that the orientation of error ellipse is a random variable with the circular standard deviation of 34° for the inner ring of targets (blue) and 22° for the outer ring (red). The two quantities were observed in the human data, averaged separately for the two rings of targets. In these simulations, we set the endpoint variabilities ($|\Sigma|^{1/2}$) to values determined by averaging participant data at both slants, separately for the inner and outer rings of targets. The predicted relative shifts for the inner ring of targets approach 1.0 for indices of anisotropy greater than 1, similar to human behavior at the inner ring. At the outer ring, the predicted relative shifts are larger than the predicted shifts for the inner ring, also similar to human behavior. Thus, the variability of error ellipse orientations explains why the pattern of shifts predicted in Figures 4 and 5 was not observed on the inner ring of targets: Although the inner-ring error distributions were significantly anisotropic, the observed shifts of aim points were

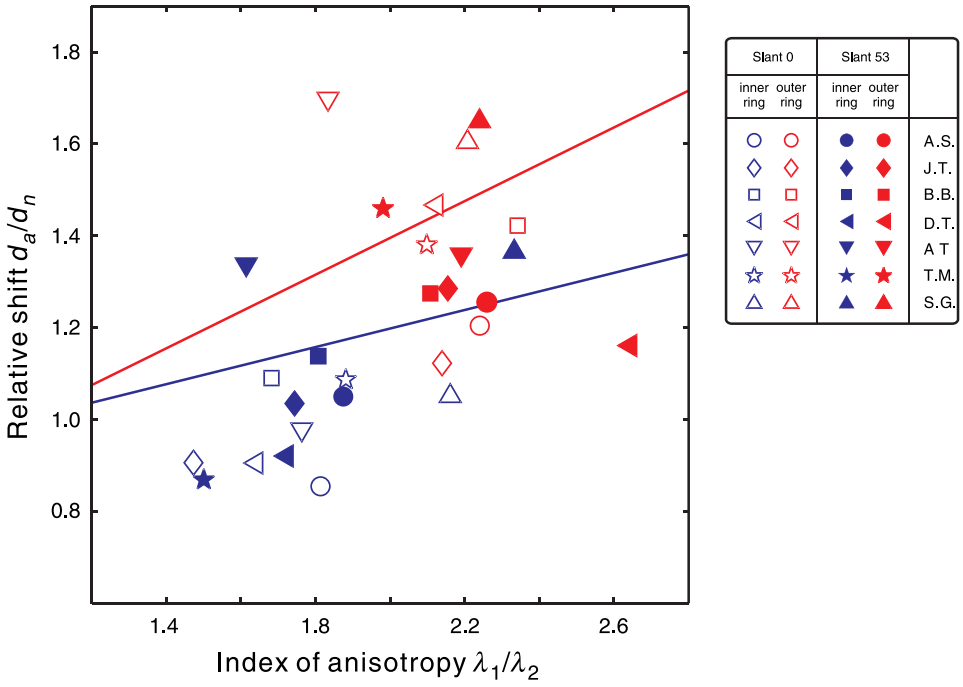

Figure 11. Effect of endpoint error anisotropy on aiming behavior. Index of anisotropy is a measure of elongation of the endpoint distribution (see Methods section). The relative shift of aim point is the ratio of the shift from the target center in the aligned condition (Figures 4A and 4D) and the shift from the target center in the nonaligned condition (Figures 4B and 4C). The larger the degree of anisotropy, the larger the relative shift of aim point (Pearson $r = .53$, $p = .004$), in agreement with predictions of the ideal planner (Figure 5B). The red and the blue lines are the relative shifts predicted by the ideal planner for the outer and the inner rings of targets, respectively. The predictions are computed as for Figure 5B, but taking into account the fact that the orientations of error ellipses are misaligned with the dock–target axis (by 34° for the inner ring of targets and by 22° for the outer ring of targets, as in the human data).

indistinguishable in the aligned and nonaligned conditions (Figure 9).

Optimality of human movement

We compared human behavior to the predictions of the ideal movement planner, based on the measured endpoint error distributions. The ideal planner shifts the aim point away from the target center, in the direction opposite of the penalty region. The amount of shift differs across targets; it depends on the size, the shape, and the orientation of the endpoint error distribution for each target.

We found good agreement between the performance of most participants and the predictions of ideal movement planner (Table 2 and Figure 12). In Figure 12, we plot the observed shifts of aim points for slant 0 as a function of the optimal shifts computed based on the endpoint variability measured for each participant in the respective condition (see Methods section). (The data for slant 53 are plotted in Figure S3.) If human aiming behavior was exactly predicted by the ideal planner, data points would fall on the main diagonal. Note that by using endpoint variability measured for each participant in the respective condition, we effectively took into account the variable orientations of error ellipses (Figure 10).

The scatter of data in Figure 12 reveals individual biases in aiming behavior. For example, at slant 0, the shifts of participant J.T. are larger than optimal, whereas the shifts of participant D.T. are smaller than optimal. We used a χ^2

	Slant 0		Slant 53	
	χ^2	p	χ^2	p
A.S.	0.89	>.999	0.84	>.999
J.T.	7.79	.932*	3.58	.999
B.B.	2.59	>.999	4.67	.995
D.T.	7.20	.952*	14.78	.468*
A.T.	9.96	.822*	11.11	.745*
T.M.	1.48	>.999	3.71	.999
S.G.	2.32	>.999	3.85	.998

Table 2. Comparison of the observed shifts of aim points with the shifts predicted by the ideal planner. The predictions were computed separately for each participant and each stimulus configuration, using measured endpoint error distributions. The p values represent the probability of obtaining a χ^2 value that is equal to or larger than the observed χ^2 value if the observed shifts did not differ from the shifts predicted by the ideal planner. The asterisks mark participants whose aiming behavior was classified as significantly different from the optimal, applying a strict criterion in our test for optimality (see text for details).

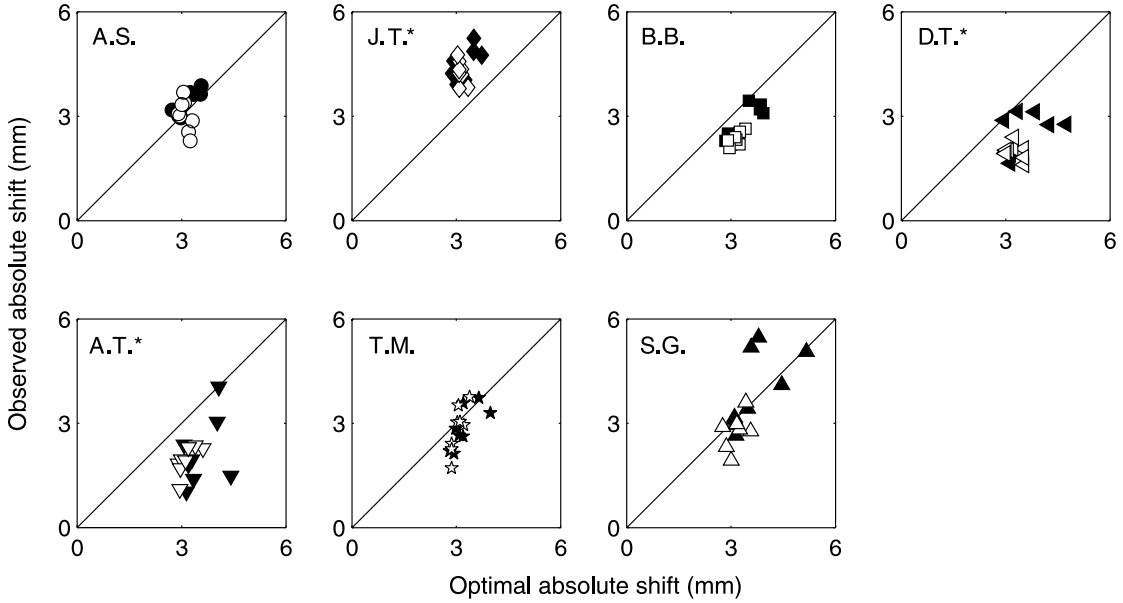

Figure 12. Observed shifts of aim point as a function of shifts predicted by the optimal planner, at slant 0. The different symbols represent different participants, as in Figure 9. The white and black symbols represent the inner-ring and the outer-ring data, respectively. If the observed behavior was identical to the predicted optimal behavior, all the symbols would fall on the diagonal line. Results of the optimality tests are reported in Table 2. The asterisks mark participants whose aiming behavior was classified as significantly different from the optimal, applying a strict criterion in our test for optimality (see text for details).

goodness-of-fit test to measure the similarity of the observed shifts and the shifts predicted by the ideal planner (Table 2). The χ^2 values were computed as follows: $\Sigma(\mu_t^{obs} - \mu_t^*)^2/|\mu_t^*|$, where μ_t^{obs} is the observed shift and μ_t^* is the shift predicted by the ideal planner. Large χ^2 values indicate large deviations from optimality. When applying the common confidence level of 95%, performance of none of our participants was classified as significantly different from optimal because all the χ^2 values were smaller than the 95% cutoff value ($\chi^2 = 25.0$). To capture the difference between participant performance evident in Figures 12 and S3, we used a more strict criterion that corresponds to the cutoff value $\chi^2 = 7.0$. By this criterion, results of three participants out of seven were classified as different from optimal for slant 0. For slant 53, results of two participants out of seven were classified as different from optimal. Thus, behavior of most participants (in 9 cases out of 13) was indistinguishable from optimal.

The above analysis of optimality is based on the shifts of aim point expressed in absolute units (mm). Significance of the same magnitude of shift expressed in absolute units is different for participants with different endpoint variability. For example, the same difference between measured and predicted performance represents a larger deviation for participants with smaller endpoint variability. To test whether our evaluation of participants' pointing performance depended crucially on our use of absolute units to measure magnitudes of aim point shifts, we normalized the difference between observed and optimal pointing behavior by the standard deviations of the endpoint error distributions (Figure 13). Results of this analysis are summarized in Table 3. The smaller "k values" indicate closer correspondence between the observed and ideal aim points. The asterisks in the columns "mean" of Table 3 are copied from Table 2; they mark those participants whose behavior was classified as suboptimal based on the results of the χ^2 goodness-of-fit test. Note that the marked k values correspond to the largest k values within their columns, indicating that performance farthest from the optimal in absolute units was also farthest from the optimal in the normalized units. Interestingly, the k values averaged within rings of targets (columns "inner ring" and "outer ring") show that in most conditions, participants' pointing behavior was closer to optimal on the outer than inner rings of targets.

We also compared human and optimal strategies in terms of the points scored during the experiment. The result is shown in Figure 14 in which the scores accumulated by humans are plotted against the predicted scores. In Table 4, we summarize performance of all the participants in terms of their shift efficiencies and gain efficiencies, which are the normalized differences of observed and predicted shifts and gains, respectively (see the Comparison of observed and optimal behavior section). Shift efficiencies ranged between 55% and 99%. Gain efficiencies ranged between 57% and 107%.[1]

These results indicate that the nervous system can represent multiple error distributions and take them into account in movement planning and execution.

We tested whether participants' aiming behavior changed over the course of the experiment by measuring

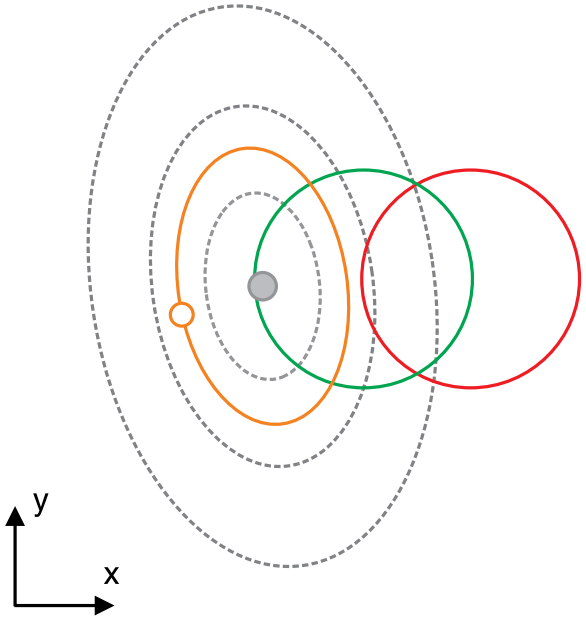

Figure 13. Measurement of the similarity of human and optimal pointing performance. The small (filled) gray circle represents the *measured aim point* (the mean of the measured endpoint distribution) and the small (unfilled) orange circle represents the *optimal prediction of the aim point* by the ideal planner. The three dashed gray ellipses around the measured aim point represent standard deviations of measured variability of endpoints. From small to large, the ellipses correspond to 1, 2, and 3 standard deviations (*SD*) of the endpoint error. To measure how far the optimal aim point is from the measured aim point, we computed a *k–SD* ellipse (shown in orange), with *k* indicating the number of standard deviations of the fitted ellipse that passes through the optimal point and whose orientation, mean, and anisotropy are the same as the measured endpoint ellipse. Thus, *k* is the distance between the measured and the predicted aim points in units of the standard deviation of the measured endpoint error. In this diagram, *k* is approximately 1.5. As before, the red and the green circles represent the penalty and the target regions. The *k* values across participants and conditions are shown in Table 3. (The diagram is a schematic representation of the stimulus and the response in arbitrary units.)

the shifts of aim points within quartiles of trials (Figures 15 and S4). Using repeated measures ANOVA, we found that only one participant significantly changed his aim point across the quartiles, participant S.G.: $F(3, 379) = 5.971$, $p = .001$ for slant 0, and $F(3, 308) = 4.696$, $p = .003$ for slant 53; all other participants: $p > .5$ for both slants. In other words, most participants maintained the same visuomotor strategies throughout the experiment, independent of whether or not the strategies were optimal.

Our finding that most participants used a stable close-to-optimal strategy in a task associated with several different error distributions should not be interpreted as evidence that the participants approached our task with correct estimates of the multiple errors distributions expected in the task. On the contrary, previous research showed that humans monitor their errors and rapidly update their representations of errors when the errors change (e.g., Figure 7 in Trommershäuser et al., 2005).

Two of the three authors (A.S., S.G.) and two of the four "naive" participants (T.M., B.B.) selected optimal strategies. Did explicit knowledge about correct strategies in our task facilitate authors' optimal performance? Our results suggest that it did not, for two reasons. First, two authors — J.T. and S.G. — started off choosing too large shifts of aim points, which led to suboptimal performance. This implies that even the participants who were aware of the hypothesis under test were not more proficient at estimating their endpoint variability than naive participants. Second, had the authors enjoyed better estimates of their task-relevant variability than naive participants, we would have seen evidence of learning in the naive participant data, but not in the author data. The opposite was the case: Neither naive participant showed significant learning, whereas one of the authors — S.G. — changed his behavior from the initial over-shifting strategy to a nearly optimal performance (Figures 15 and S4).

Our results suggest why human performance deviated from optimal. In most conditions, human performance was closer to optimal on the outer than inner rings of targets (Table 3). It is plausible that the differences in performance stemmed from the fact that the anisotropy of measured endpoint distributions was larger on the outer than the inner ring (Tables 1 and S1), so participants' ability to represent the shapes of endpoint distributions and use the representations in movement planning was better for conditions where the evidence of anisotropy was stronger, that is, on the outer ring.

Discussion

Summary

We studied human movement planning under risk during sequences of rapid pointing movements. The characteristics of uncertainty (i.e., the shapes and the sizes of endpoint error distributions) varied across the subsequent movements. At two different slants of the touch screen, humans performed rapid goal-directed pointing movements toward stimulus configurations in different directions and at different eccentricities from a starting position at screen center. Stimulus configurations consisted of two partially overlapping regions. Hits inside the target region increased the cumulative score; hits inside the penalty region decreased the score.

The shapes and the sizes of measured endpoint error distributions varied across pointing locations. Endpoint errors along the direction of movement increased with distance from the center, leading to an elongation of

	Slant 0			Slant 53		
	Mean	Inner ring	Outer ring	Mean	Inner ring	Outer ring
A.S.	0.4267	0.5263	0.3270	0.4014	0.4976	0.3052
J.T.	0.7407*	0.8075	0.6738	0.4968	0.5042	0.4894
B.B.	0.3694	0.4385	0.3002	0.4641	0.5188	0.4093
D.T.	0.5461*	0.6265	0.4658	0.6449*	0.7519	0.5379
A.T.	0.6551*	0.6754	0.6348	0.6719*	0.6535	0.6902
T.M.	0.5261	0.6434	0.4088	0.4875	0.5747	0.4004
S.G.	0.4773	0.5243	0.4303	0.5228	0.5042	0.5414

Table 3. Similarity of human and optimal pointing performance. Each value indicates the distance between the measured aim point and the aim point predicted by the ideal planner, expressed in units of standard deviation of the measured endpoint error distribution (k in Figure 13). The smaller the k value, the closer human performance is to the optimal prediction. The different columns are obtained by averaging k values across different spatial target locations, for every participant and slant: averaged across all the conditions in the "mean" columns, and across the inner ring (Targets 1–4) and the outer ring (Targets 5–8) of targets in the "inner ring" and "outer ring" columns, respectively. The asterisks in the "mean" columns are the same as in Table 2; they mark those participants whose behavior was classified as significantly different from optimal based on the results of the χ^2 goodness-of-fit test.

endpoint distributions in movement direction. Participants were able to take into account these changes in endpoint error distributions. The aim points shifted away from the target center, in opposite direction from the penalty region. Moreover, for the same target location, shifts were larger in the direction of larger endpoint variability, indicating that participants took into account the anisotropy of the endpoint errors. In nine out of 14 cases, human performance was indistinguishable from optimal performance predicted by an ideal movement planner maximizing expected gain (Table 2). The observed aim points were stable throughout the experiment for most participants, indicating that participants maintained the same visuomotor strategy throughout the experiment.

Taken together, these results suggest that participants use their estimates of motor uncertainty in movement planning.

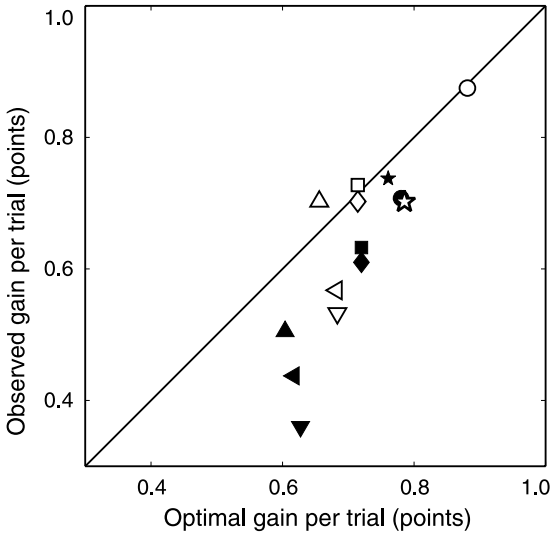

Figure 14. Measured gains as a function of the gains predicted by the ideal planner, at slant 0. The different shapes of symbols represent different participants (the same as in the previous figures). The white and black symbols represent the inner-ring and the outer-ring data, respectively. If the observed score was identical to the predicted optimal score, all the symbols would fall on the diagonal line. We report the correspondence between the observed data and predictions of the ideal planner by computing gain efficiencies for both slants in Table 4.

Sources of sensorimotor variability

We investigated the effect of sensorimotor variability on human motor behavior by varying three parameters in our task: The movement direction and the distance, and the slant of the surface to which the movements were directed.

	Gain efficiency		Shift efficiency	
	Slant 0	Slant 53	Slant 0	Slant 53
A.S.	0.99	0.91	0.97	0.98
J.T.	0.98	0.85	0.63*	0.87
B.B.	1.02	0.88	0.79	0.75
D.T.	0.83	0.71	0.66*	0.55*
A.T.	0.78	0.57	0.61*	0.59*
T.M.	0.89	0.97	0.91	0.81
S.G.	1.07	0.84	0.99	0.91

Table 4. Efficiency of human behavior expressed in terms of gains earned by the participants ("gain efficiency") and shifts of aim points ("shift efficiency"), calculated separately for each participant and slant. We estimated shift (gain) efficiency by taking the ratio of observed to ideal shifts (gains per trial). The asterisks in the shift-efficiency columns are the same as in Table 2; they mark the conditions in which human data are classified as significantly different from the predictions of the ideal planner.

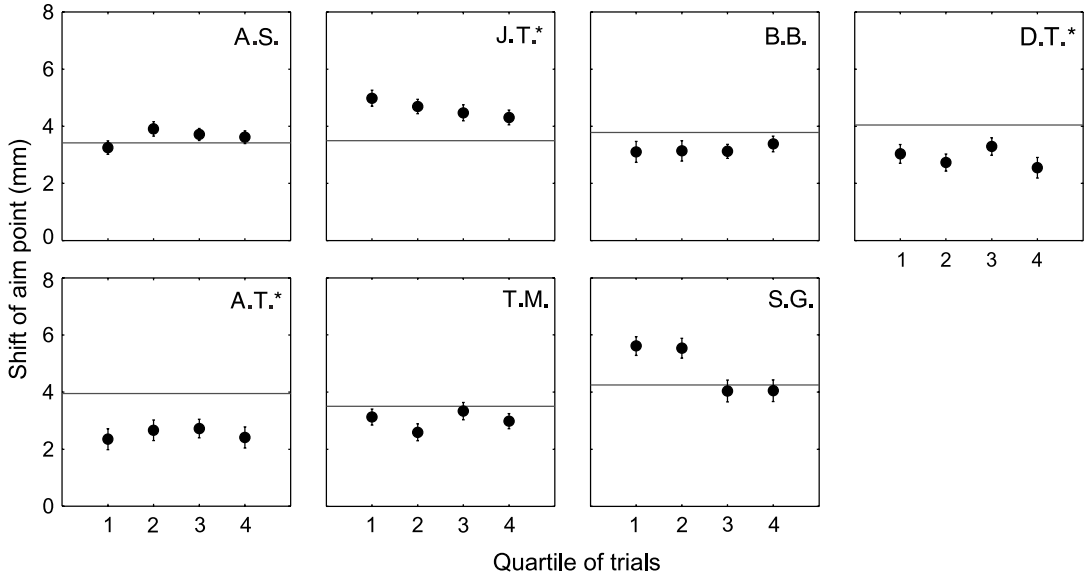

Figure 15. Observed individual shifts of aim points within quartiles of trials, in the aligned conditions on the outer ring of targets for slant 0. The observed shifts remained roughly constant for all but one participant (S.G.). Error bars indicate two standard errors of the estimates of aim point shifts within the quartiles. Horizontal lines represent the optimal shifts predicted by the ideal planner for these conditions, based on the individual endpoint distributions averaged across the quartiles. (The data for slant 53 appear in Figure S4.)

Of the three parameters, movement direction and distance strongly affected the distribution of movement errors, whereas slant had a negligible effect. These results agree with the results of previous studies in which motor errors have been found to increase with movement amplitude and speed (Fitts, 1954; Fitts & Petersen, 1964; Gordon et al., 1994; Harris & Wolpert, 1998; Meyer, Abrams, Kornblum, Wright, & Smith, 1988; Plamondon & Alimi, 1997; Schmidt, Zelaznik, Hawkins, Frank, & Quinn, 1979; Woodworth, 1899). In our task, movement amplitude and average movement speed were larger for movements directed at stimuli on the outer ring than to the inner ring. Consistently, endpoint error ellipses were larger on the outer than on the inner ring.

We found that outer-ring error distributions were more anisotropic than inner-ring distributions. This is in contrast to results of Gordon et al. (1994), who found larger error anisotropy in short-range than in long-range movements. In the experiment of Gordon et al., participants did not receive feedback about the position of the cursor during movement. Thus, participants could not correct the errors they made at movement onset, and the directional error increased proportionally with movement amplitude. In our task, participants had clear vision of their hands, so that they could correct for deviations from the dock-to-target line throughout movement. Still the extent error increased substantially with movement amplitude under these conditions, leading to more anisotropic endpoint distributions for movements toward target locations on the outer ring.

Peripheral presentation of our stimuli might also have contributed to the endpoint error in our task because sensory noise is generally larger for stimuli presented in visual periphery (Carrasco & Yeshurun, 1998; Eckstein, Thomas, Palmer, & Shimozaki, 2000). This seems unlikely, however, in light of recent eye-movement measurements by Stritzke and Trommershäuser (2007). In a speeded pointing task, using stimuli and presentation durations similar to ours, these authors showed that humans make on average two saccades toward the stimuli, while the second saccade was completed approximately 300 ms prior to arrival of the hand to the stimulus. The eye movement brought visual stimuli into the range of parafoveal vision, giving the visual system sufficient time to estimate parameters of the visual configuration.

In our task, stimuli presented at slant 53 spanned a larger range of depths than at slant 0. Precision of binocular vision is known to deteriorate with binocular disparity (e.g., McKee, Levi, & Bowne, 1990). However, we cannot attribute the small differences we found between the endpoint distributions at the two slants to differences in binocular disparities because the eye movements were likely to bring our stimuli into the range of similarly small binocular disparities across all conditions. The slightly larger observed endpoint variability for slant 53 than for slant 0 was probably due to the more difficult movements at slant 53 than slant 0. Our participants typically chose a less comfortable hand posture at slant 53 than slant 0 because their hand occluded more of the screen at slant 53 than at slant 0.

We conclude that the differences in endpoint variability across target locations in our task depended more on motor than sensory uncertainty.

Parallel vs. serial representation of uncertainty

Natural actions typically involve sequences of movements in different directions and with different amplitudes. To optimize motor behavior, movement planning should take into account the different uncertainties of each movement in the sequence, and it should be able to access the different representations in rapid succession. Our results show that the human nervous system can represent several endpoint error distributions for movements carried out in rapid succession. We do not know, however, whether these distributions are represented concurrently (in parallel), or whether the planning mechanism rapidly switches from one representation to another (i.e., it accesses representations serially), as the parameters for executing the next movement need to be defined. Evidence from visual perception suggests that the nervous system fails to reliably represent more than one representation of task-relevant uncertainty at once (e.g., Gorea & Sagi, 2000).

Further studies will show whether this constraint generalizes to motor planning. The possibility that the motor system fails to maintain several parallel representations of uncertainty, and rapidly switches to the relevant representation every time a new movement goal is set, raises many interesting questions about the mechanism of switching between representations.

Acknowledgments

We thank Laurence T. Maloney and Joshua A. Solomon for discussions, David C. Knill and Michael S. Landy for comments on an earlier version of the manuscript, Peter Jurica for help in optimizing simulations of the ideal planner, and Diana Pittig for assistance with data collection. This research was partly supported by Deutsche Forschungsgemeinschaft (DFG), Grant TR 528/1-2; 1-3. A part of this study was presented at the 29th European Conference on Visual Perception in St.-Petersburg, August 2006.

Commercial relationships: none.
Corresponding author: Sergei Gepshtein.
Email: sergei@brain.riken.jp.
Address: Laboratory for Perceptual Dynamics, Computational Neuroscience Group, Brain Science Institute, RIKEN, 2-1 Hirosawa, Wakoushi, Saitama 351-0198, Japan.

Footnote

[1]In a single experiment, observed gain efficiency may be greater than 1 due to luck and chance, when the signed differences between observed and predicted gains are used to compute gain efficiency, as we did presently. Another measure of efficiency is often reported, where absolute–rather than signed–differences between observed and predicted values are used to compute efficiency. If the latter measure is used for our data (i.e., defining gain efficiency as $1 - |G_{obs} - G_{opt}|/G_{opt}$), the results remain the same as reported in Table 4 for all conditions except for observers B. B. and S. G. at slant 0, where gain efficiencies become 0.98 and 0.93, respectively.

References

Alais, D., & Burr, D. (2004). The ventriloquist effect results from near-optimal bimodal integration. *Current Biology, 14,* 257–262. [PubMed] [Article]

Carrasco, M., & Yeshurun, Y. (1998). The contribution of covert attention to the set-size and eccentricity effects in visual search. *Journal of Experimental Psychology: Human Perception and Performance, 24,* 673–692. [PubMed]

Diedrichsen, J., Hashambhoy, Y., Rane, T., & Shadmehr, R. (2005). Neural correlates of reach errors. *Journal of Neuroscience, 25,* 9919–9931. [PubMed] [Article]

Eckstein, M. P., Thomas, J. P., Palmer, J., & Shimozaki, S. S. (2000). A signal detection model predicts the effects of set size on visual search accuracy for feature, conjunction, triple conjunction, and disjunction displays. *Perception & Psychophysics, 62,* 425–451. [PubMed]

Ernst, M. O., & Banks, M. S. (2002). Humans integrate visual and haptic information in a statistically optimal fashion. *Nature, 415,* 429–433. [PubMed]

Fisher, N. I. (1993). *Statistical analysis of circular data.* New York: Cambridge University Press.

Fitts, P. M. (1954). The information capacity of the human motor system in controlling the amplitude of movement. *Journal of Experimental Psychology, 47,* 381–391. [PubMed]

Fitts, P. M., & Peterson, J. R. (1964). Information capacity of discrete motor responses. *Journal of Experimental Psychology, 67,* 103–112. [PubMed]

Gepshtein, S., & Banks, M. S. (2003). Viewing geometry determines how vision and haptics combine in size perception. *Current Biology, 13,* 483–488. [PubMed] [Article]

Gordon, J., Ghilardi, M. F., & Ghez, C. (1994). Accuracy of planar reaching movements: I. Independence of direction and extent variability. *Experimental Brain Research, 99,* 97–111. [PubMed]

Gorea, A., & Sagi, D. (2000). Failure to handle more than one internal representation in visual detection tasks. *Proceedings of the National Academy of Sciences of*

the United States of America, 97, 12380–12384. [PubMed] [Article]

Harris, C. M., & Wolpert, D. M. (1998). Signal-dependent noise determines motor planning. *Nature, 394,* 780–784. [PubMed]

McKee, S. P., Levi, D. M., & Bowne, S. F. (1990). The imprecision of stereopsis. *Vision Research, 30,* 1763–1779. [PubMed]

Meyer, D. E., Abrams, R. A., Kornblum, S., Wright, C. E., & Smith, J. E. (1988). Optimality in human motor performance: Ideal control of rapid aimed movements. *Psychological Review, 95,* 340–370. [PubMed]

Plamondon, R., & Alimi, A. M. (1997). Speed/accuracy trade-offs in target-directed movements. *Behavioral and Brain Sciences, 20,* 279–349. [PubMed]

Scheidt, R. A., Conditt, M. A., Secco, E. L., & Mussa-Ivaldi, F. A. (2005). Interaction of visual and proprioceptive feedback during adaptation of human reaching movements. *Journal of Neurophysiology, 93,* 3200–3213. [PubMed] [Article]

Schmidt, R. A., Zelaznik, H., Hawkins, B., Frank, J. S., & Quinn, J. T., Jr. (1979). Motor-output variability: A theory for the accuracy of rapid motor acts. *Psychological Review, 86,* 415–451. [PubMed]

Stritzke, M., & Trommershäuser, J. (2007). Eye movements during movement under risk. *Vision Research, 47,* 2000–2009. [PubMed]

Trommershäuser, J., Gepshtein, S., Maloney, L. T., Landy, M. S., & Banks M. S. (2005). Optimal compensation for changes in task relevant movement variability. *Journal of Neuroscience, 25,* 7169–7178. [PubMed] [Article]

Trommershäuser, J., Maloney, L. T., & Landy, M. S. (2003). Statistical decision theory and the selection of rapid, goal-directed movements. *Journal of the Optical Society of America A, Optics, image science, and vision, 20,* 1419–1433. [PubMed]

van Beers, R. J., Haggard, P., & Wolpert, D. M. (2004). The role of execution noise in movement variability. *Journal of Neurophysiology, 91,* 1050–1063. [PubMed] [Article]

Woodworth, R. S. (1899). The accuracy of voluntary movement. *Psychology Monographs, 3,* 2.